frontiers in Materials

ORIGINAL RESEARCH
published: 08 April 2021
doi: 10.3389/fmats.2021.635987

Reduced Graphene Oxide-Poly (Ionic Liquid) Composite Films of High Mechanical Performance

Jian Chang[1], **Xianjing Zhou**[2], **Qiang Zhao**[3], **Wei Cao**[1], **Miao Zhang**[1]* and **Jiayin Yuan**[1]*

[1] Department of Materials and Environmental Chemistry, Stockholm University, Stockholm, Sweden, [2] Department of Chemistry, Zhejiang Sci-Tech University, Hangzhou, China, [3] Key Laboratory of Material Chemistry for Energy Conversion and Storage (Ministry of Education), School of Chemistry and Chemical Engineering, Huazhong University of Science and Technology, Wuhan, China

Graphene and its derivatives are a classical group of two-dimensional (2D) building blocks possessing excellent mechanical and/or electrical properties in favor of preparing flexible electronic devices. Natural materials, such as nacre, provide inspiration and an exciting guideline for assembling 2D nanosheets into functional nanocomposites. In this context, despite recent advance, methods to assemble graphene-derived nanosheets into nanocomposites with the integrated enhancement of mechanical properties and electrical conductivity are eagerly pursued. Here, a rational design has been proposed and demonstrated, which utilizes synergistic supramolecular interactions between a polymeric additive and reduced graphene-oxide nanosheets to fabricate exceptional, integrated, strong, and tough nanocomposite films with high electrical conductivity. Such materials can be applied in areas such as, aerospace, artificial muscle, tissue engineering, and flexible electronics.

Keywords: reduced graphene oxide, π-π interaction, cation-π interaction, high mechanical performance, poly (ionic liquid)

Edited by:
Mazeyar Parvinzadeh Gashti,
PRE Labs Inc., Canada

Reviewed by:
Pingan Song,
University of Southern Queensland, Australia
Mohammad Arjmand,
University of British Columbia Okanagan, Canada

Correspondence:
Miao Zhang
miao.zhang@mmk.su.se
Jiayin Yuan
jiayin.yuan@mmk.su.se

Specialty section:
This article was submitted to Polymeric and Composite Materials, a section of the journal Frontiers in Materials

Received: *30 November 2020*
Accepted: *15 March 2021*
Published: *08 April 2021*

Citation:
Chang J, Zhou X, Zhao Q, Cao W, Zhang M and Yuan J (2021) Reduced Graphene Oxide-Poly (Ionic Liquid) Composite Films of High Mechanical Performance. Front. Mater. 8:635987. doi: 10.3389/fmats.2021.635987

INTRODUCTION

Graphene and its derivatives, such as reduced graphene oxide (rGO) and graphene nanoribbon, such as classic two-dimensional (2D) nanomaterials have been considered as a promising candidate to fabricate flexible electronic devices, such as touch screen and wearable sensor (Wang and Shi, 2015), owing to their exceptional electrical and mechanical properties (Cheng et al., 2015; Zhang et al., 2016). Inspired by the wisdom of mother nature to build up nacre (Barthelat et al., 2016), efforts have been devoted to assembling microscopic 2D nanosheets into macroscopic nanocomposites *via* the assistance of additives, such as chemical or physical crosslinkers ranging from polymers to metal ions (Park et al., 2008; Zhao et al., 2016; Wang et al., 2018; Li et al., 2019). In particular, polymer additives have been demonstrated for integrated strength and toughness in the nanocomposites *via* a variety of interfacial interactions, such as hydrogen bonding (Liu et al., 2013; Wang et al., 2015; Wan et al., 2016), electrostatic interaction (Kulkarni et al., 2010; Tan et al., 2015), π-π interaction (Zhang et al., 2014; Song et al., 2017), and covalent crosslinking (Cheng et al., 2013; Cui et al., 2014; Woo et al., 2019). Previously, methods are proposed to use polymer crosslinkers to reinforce the inter-layer interactions after postreduction of graphene oxide (GO), while efforts suffer from the limited interaction sites on rGO, since most oxygenated moieties on GO sheets upon reduction are removed. Meanwhile, the insertion of insulating polymers would also deteriorate electrical property of rGO film because the formation of bulk polymer domains would disturb the regular packing of rGO nanosheets and weaken electron transportation between rGO interlayers. Therefore, challenges remain for fabricating strong, tough, and highly conductive rGO-based nanocomposites.

Recently, "cation–π" interaction, which is a popular example of supramolecular interactions, has been exploited as a useful physical crosslinking model, arising from an electrostatic interplay between a cation and the π electron cloud of an aromatic system. The strength of the cation–π interaction can be even stronger than other types of noncovalent interactions (Zhao and Zhu, 2020), which is of great significance in membrane structural stability and interlayer spacing control. Therefore, polymers carrying cations could be accessible to construct rich cation–π interactions with the delocalized polarizable π electrons of rGO sheets, thereby capable of improving the mechanical performance of nanocomposites. In addition, the aromatic functionality could also be molecularly involved into polymeric crosslinking strategy because it can initiate π-π interaction with the natural aromatic structure of rGO sheets, leading to improved mechanical properties (Huang et al., 2018, 2019; Xu et al., 2018).

Herein, we designed rGO-poly (ionic liquid) nanocomposite films that simultaneously exhibit excellent mechanical performance and high electrical conductivity. The involved poly (ionic liquid) is an imidazolium-type polycation and carries a phenyl moiety in the repeating unit. Such structure motif enables synergistic effects of both cation–π and π-π interactions with rGO nanosheets, leading to high tensile strength of 516 ± 22 MPa and toughness of 12.16 ± 1.31 MJ m^{-3}, as well as an excellent electrical conductivity of 476 ± 30 S cm^{-1}, respectively.

MATERIALS AND METHODS

Chemicals and Materials

Graphite powder (325 mesh) was obtained from Tsinghua University (Beijing, China). 2,2′-Azobis(2-methylpropionitrile) (AIBN), 2,6-di-*tert*-butyl-4-methylphenol (DBMP), potassium permanganate, 1-vinylimidazole, tetrahydrofuran (THF), benzyl chloride, and hydrogen peroxide (30% in water) were purchased from Sigma-Aldrich. Diethyl ether (>99.8%) was purchased from Honeywell Corporation. Sulphuric acid (95%), hydroiodic acid (57%), ethanol, methanol, and acetone were purchased from VWR International Ltd. Hydrochloric acid (37%) was purchased from Fisher Chemical. Methyl sulfoxide-d_6, for nuclear magnetic resonance (NMR) measurements was purchased from Acros Organics. Poly(vinylidene fluoride) (PVDF) hydrophilic membrane (diameter = 47 mm, pore size = 0.22 μm) was purchased from Merck Millipore. All the chemicals were of analytical grade without further purification. Deionized water purified by a Milli-Q system was used in all experiments.

Characterizations

Proton Nuclear Magnetic Resonance (^{1}H NMR) spectra were recorded on Bruker Avance III 400 MHz. Gel permeation chromatography (GPC) was performed using NOVEMA Max linear XL columns with a mixture of 80% of aqueous acetate buffer and 20% of methanol. Conditions for GPC are as follows: flow rate 1.00 ml min^{-1}, PSS polymer standards using refractive index (RI) detector—Optilab-DSP-Interferometric Refractometer (Wyatt Technology Croporation, CA, USA). X-ray photoelectron spectroscopy (XPS) analysis was carried out by Thermo Escalab 250XI under ultrahigh vacuum conditions in the range of $\sim 10^{-10}$ mbar by using a monochromatic Al Kα X-ray source ($h\upsilon = 1486.6$ eV) operated at 150 W. Fourier transform infrared (FTIR) spectroscopy was carried out on IR spectrometer (670-IR). Background and sample scan times were set to 16 and samples were gently ground in a mortar prior to the measurement. X-ray diffraction (XRD) was performed on a Panalytic X'Pert Pro (Malvern Panalytical, Malvern, UK) utilizing non-monochromatic Cu Kα radiation. An acceleration voltage of 40 kV, current of 40 mA and step-size of 0.033° were used for each analysis and data were collected from 5° to 40°. The Raman spectra were collected on a LabRAM HR800 Raman spectrometer (Horiba, Villeneuve-d'Ascq, France). Scanning electron microscopy (SEM) was performed on a JSM-7000F microscope (JEOL, Tokyo, Japan). Samples were attached onto an aluminum substrate using double-sided carbon adhesive tape, and were imaged and analyzed at 10 kV. Non-conducting samples were sputtered with gold before characterization. Atomic force microscopy (AFM) was performed on Multimode AFM (Veeco Metrology, Santa Barbara, USA). The electrical conductivities were tested by multifunction digital four-probe tester (Hefei Kejing Materials Technology Co., Ltd., Anhui, China). Details of the mechanical tests are as follows: All the specimens for mechanical testing were cut into rectangular strips with a width of 3 mm and length of 30 mm, by a razor blade. Mechanical tensile tests were conducted on an Instron 5,960 universal testing machine (Instron, MA, USA). The thickness of the specimens was confirmed by measuring the cross-section of the stripped specimens. Tensile strength and failure strain were recorded when the fracture occurred. Young's modulus was calculated from the slope of the linear region of the stress–strain curves and fracture toughness is calculated by integrating the areas under the stress–strain curves. All the reported data were the average of over four strips of the same samples. The dynamic mechanical properties of composite were measured by DMA850, a dynamic mechanical thermal analyzser (DMTA) (TA Instruments, DE, USA).

Synthesis of 1-Benzyl-3-Vinylimidazolium Chloride (IL) Monomer

A mixture of 1-vinylimidazole (18.82 g, 0.20 mol) and 40 ml ETOH was added into a 500 ml round-bottom flask, accompanied with 2,6-di-tert-butyl-4-methylphenol (100 mg, 0.45 mol) as the stabilizer. Then, benzyl chloride (28 g, 0.22 mol) was slowly added into the solution. The reaction was stirred at room temperature for 1 h and then at 60°C for 1 h. After that, the oily product (20.81 g) was obtained by separation from the reaction mixture and washing with 3 × 500 ml diethyl ether and dried *via* high vacuum at 40°C (Yield: 47%).

Synthesis of Poly(1-benzyl-3-Vinylimidazolium Chloride) (PIL)

IL monomer (20 g) and the AIBN initiator (200 mg, 1 wt%) as initiator were dissolved in degassed DMF solution (200 ml) under nitrogen. Then, the reaction mixture was stirred, heated to and kept at 70°C for 24 h under nitrogen atmosphere. Afterwards, the solution was dropped into excessive acetone and the obtained precipitate was filtered off, and washed with acetone for three times. Yellow powders (12.10 g, yield: 60.5%) were obtained after vacuum-drying process at 50°C for 12 h.

Synthesis of 3-Cyanomethyl-1-Vinylimidazolium Bromidemonomer (CMVImBr)

1-Vinylimidazole (10 g) and bromoacetonitrile (15 g) were dissolved in 125 ml THF. It is to be noted there should be any direct mixture of 1-vinylimidazole and bromoacetonitrile. The reaction mixture was stirred and heated in an oil bath at 60°C for 12 h. The obtained precipitate was filtered off, washed with THF for three times and dried by high vacuum at 50°C for 12 h (Yield: 87%).

Synthesis of Poly(3-Cyanomethyl-1-Vinylimidazolium Bromide) (PILC)

CMVImBr monomer (10 g) and AIBN initiator (80 mg) were dissolved in degassed DMSO (100 ml) under nitrogen. The reaction mixture was stirred, heated to and kept at 60°C for 12 h under nitrogen atmosphere. Afterwards, the solution was dropped into excessive THF (1 L). The obtained precipitate was collected by filtration, washed with THF three times and vacuum-dried at 50°C for overnight (Yield: 51%).

Preparation of GO

Graphite powder (1 g, 325 mesh) was added slowly into 95% sulphuric acid (30 ml) into a 250 ml flask. The reaction slurry was vigorously stirred at 20°C for 30 min. Potassium permanganate (3.0 g) was added slowly into the slurry *via* further stirring for over 10 min and the oxidation reaction was performed more than 3 h at 20°C. Then the reaction was terminated by pouring the reaction system into 500 ml deionized water at 20°C, and 10 ml H_2O_2 aqueous solution (30 wt%) was slowly added to reduce Mn(VII) species. Graphite oxide was obtained by separation from the reaction system *via* centrifugation at 10,000 rpm for 40 min. The obtained graphite oxide was washed with 1,000 ml aqueous HCl solution (v/v = 1/10 from 37% concentrated HCl aqueous solution and deionized water) for three times *via* centrifugation at 10,000 rpm for 50 min. After washing with deionized water for another three times, the graphite oxide dispersion was exfoliated by mild sonication (input energy $< 30\,\mathrm{J\ L^{-1} s^{-1}}$) at 20°C for 10 min. Afterwards, the GO dispersion was performed to another three cycles of centrifugation at 3,000 rpm (30 min for each) to remove the graphite powder and unexfoliated graphite oxide agglomerates. Finally, the dilute GO dispersion was concentrated again by centrifugation at 10,000 rpm for 50 min, which generates the GO stock.

Preparation of the GO Composite Films (GO/PIL-*x*%)

The GO stock was diluted by deionized water and treated by 10 min mild sonication plus 10 min stirring. PIL was dissolved in deionized water at a defined concentration. Then, a defined amount of PIL aqueous solution (the mass of PIL is 1.0–5.0 wt% relative to GO) was added dropwise into the GO dispersion and stirred for 1 h followed by sonication for 10 min to obtain a homogeneous dispersion. After homogenization, the obtained dispersion was vacuum-filtered off into a composite film on a PVDF filtration support termed GO/PIL-***x***% (x = 1 to 5). A free-standing GO/PIL-***x***% was easily peeled off from the PVDF filter support.

Preparation of rGO Film and rGO-Based Composite Films (rGO/PIL-*x*%)

The reduction of the GO film and GO/PIL-***x***% films was performed in 15 wt% hydroiodic (HI) acid aqueous solution at 20°C for 12 h. Then they were washed repeatedly by ethanol to remove I_2 adsorbed on the rGO and rGO/PIL-***x***% films.

RESULTS AND DISCUSSION

The preparation of rGO/PIL nanocomposite films is schematically illustrated in **Figure 1**. The monomer1-benzyl-3-vinylimidazolium chloride, termed IL, carrying simultaneously an imidazolium and a phenyl functionality was synthesized through a one-step quaternization reaction of 1-vinyl imidazole with benzyl chloride; IL was then radically polymerized (**Figure 1**) to poly(1-benzyl-3-vinylimidazolium chloride), abbreviated here as PIL (Men et al., 2013; Grygiel et al., 2015; Shao et al., 2020; Wang et al., 2020; Zhang et al., 2020). Its chemical structure and macromolecular features were characterized and confirmed by proton nuclear magnetic resonance (^{1}H NMR) spectroscopy and gel permeation chromatography (GPC), respectively (**Supplementary Figures 1**, **2**). In this study, GO nanosheets were synthesized *via* a modified Hummers' method by a mild room-temperature oxidation reaction of nature graphite (Chen et al., 2019). Next, the exfoliated GO nanosheets were dispersed in deionized (DI) water and mixed with the PIL aqueous solution upon sonication. The obtained homogeneous dispersion was filtered off into a GO/PIL nanocomposite film on a porous hydrophilicpoly(vinylidene difluoride) (PVDF) substrate *via* a pressure-assisted filtration method. Finally, the GO/PIL nanocomposites were chemically reduced by HI acid (), in which GO recovered most of the conjugated structure of the graphitic phase to become rGO. Here, a series of GO/PIL nanocomposites with varied PIL contents were fabricated and termed GO/PIL-***x***%, where ***x***% denotes the relative mass amount of PIL to GO; correspondingly, their reduced counterparts were termed rGO/PIL-***x***%. To note, there exists multiple inter-molecular interactions in rGO/PIL-***x***% between PIL and rGO nanosheets (**Figure 1**). Specifically, in the rGO/PIL composite, the HI reduction of the carboxylate and hydroxyl groups on GO surface could in large part reduce the imidazolium-carboxylate based electrostatic attraction and the hydrogen bonding between PIL and rGO sheet. Besides, the aromatic phenyl groups in PIL and the π-conjugated domains of rGO will facilitate the π-π interactions; the imidazolium cation can operate the cation–π attraction with all these aromatic moieties. Both the π-π and

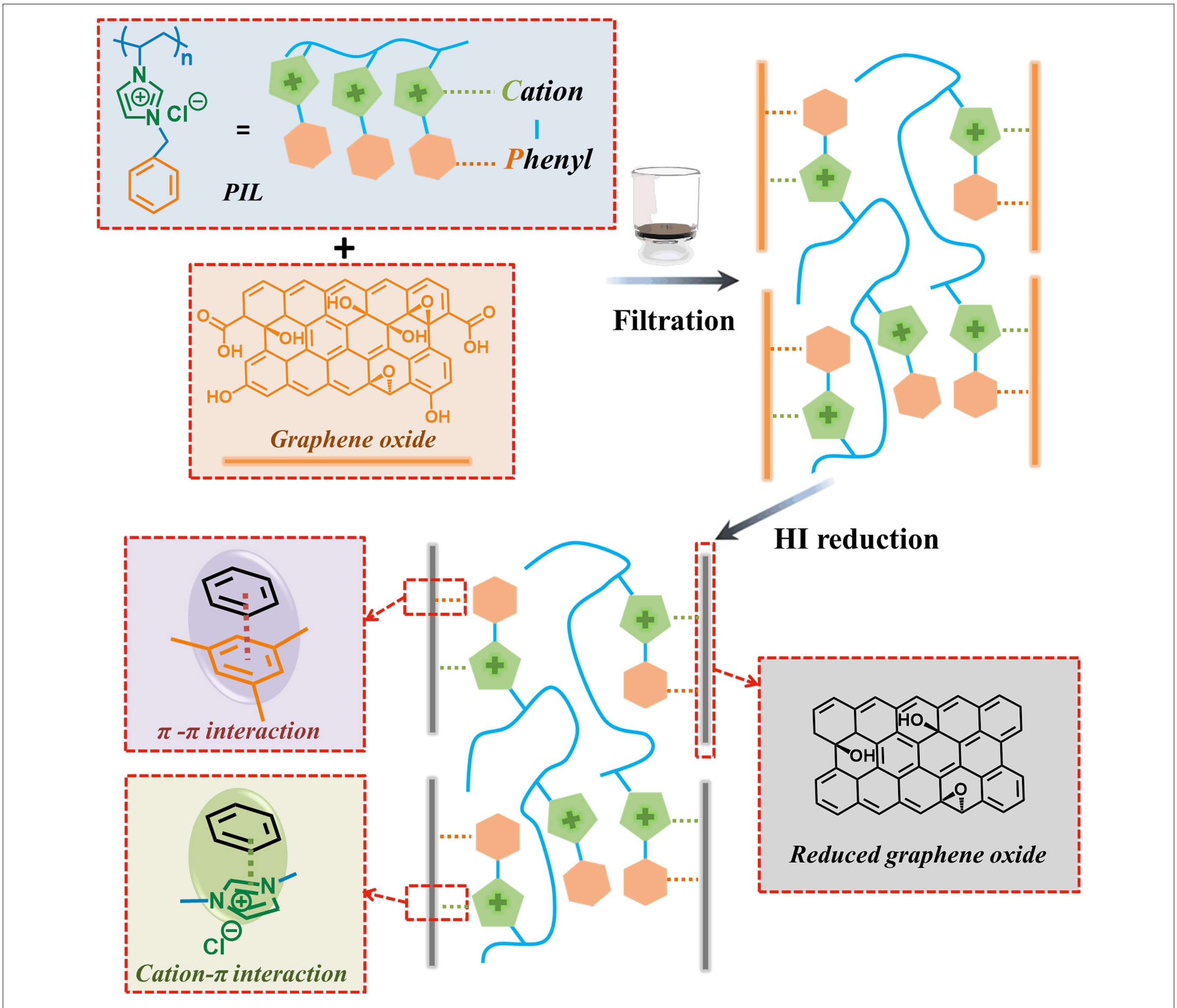

FIGURE 1 | Schematic illustration of the preparation procedure of the target rGO/PIL nanocomposite film and relevant interface interactions in it. rGO, reduced graphene oxide; PIL, poly(1-benzyl-3-vinylimidazolium chloride).

the cation–π interactions between PIL and rGO dominate in the composite. In addition, the π-π interaction between adjacent rGO sheets could be strengthened duo to the partial recovery of π-conjugated networks.

The surface morphology, lateral size and thinness of the pristine GO nanosheets were analyzed first by atomic force microscopy (AFM) and scanning electron microscope (SEM) tests. As presented in **Supplementary Figure 3**, the exfoliated GO nanosheets possess an average lateral size of 2.41 ± 1.30 μm, a thinness of 0.79 ± 0.07 nm, and intrinsic wrinkle morphology on their basal planes due to the sp^3-hybridized structural defects (**Figure 2A**; Schniepp et al., 2006; Zhang et al., 2014, 2015). After re-organization of GO nanosheets into GO/PIL nanocomposites, the surface roughness was changed and dependent on the added PIL content. Among these samples, GO/PIL-3% displays the most wrinkled texture with an enhanced roughness of 24.48 ± 4.09 nm in an area of 5 × 5 μm^2 in comparison with the pristine GO film (18.18 ± 1.67 nm). The enhanced roughness is presumably due to strong GO-PIL interactions as well as the film drying process (**Figure 2B**; **Supplementary Figure 4**). In contrast, upon reduction of HI, the roughness shrinks sharply to 10.00 ± 0.47 nm for rGO/PIL-3% and 8.35 ± 2.09 nm for the PIL-free rGO film in an area of 5 × 5 μm^2, as shown in **Supplementary Figure 5**.

Undoubtedly, the films of GO, rGO, GO/PIL-3%, and rGO/PIL-3% all present a typical laminated profile in their cross-sectional SEM images (**Supplementary Figure 6**), as expected from the packing of 2D building units. The laminated packing

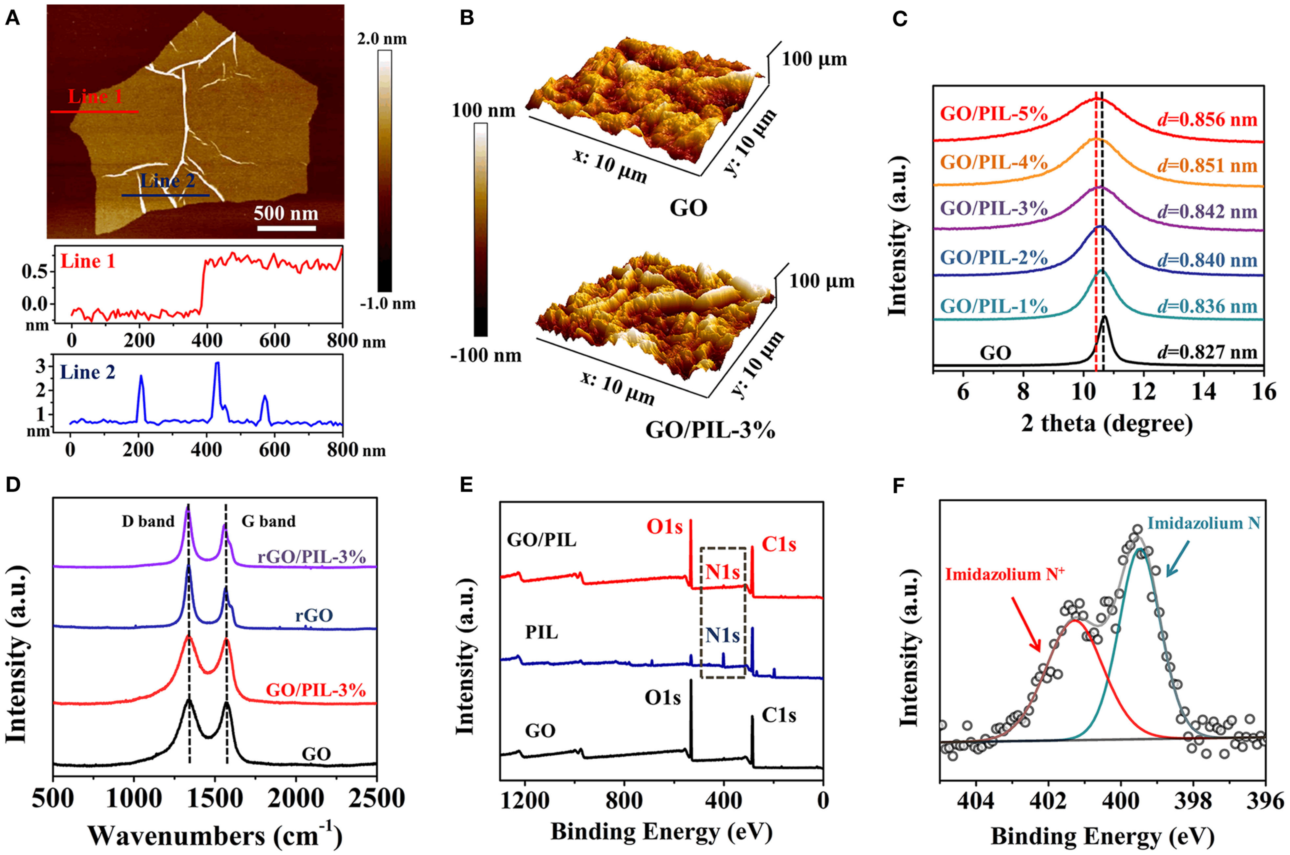

FIGURE 2 | (A) A representative AFM image of the prepared GO sheet and its corresponding height profile. **(B)** 3D AFM images of the pristine GO film (top) and GO/PIL-3% (bottom). **(C)** XRD patterns of the pristine GO film and GO/PIL-***x***%, ***x*** = 1 to 5. **(D)** Raman spectra of GO, GO/PIL-3%, rGO and GO/PIL-3% films. **(E)** XPS spectra of the pristine GO film, PIL, and GO/PIL-3%. **(F)** The high resolution spectrum of N1s of GO/PIL-3%. AFM, Atomic force microscopy; PIL, poly(1-benzyl-3-vinylimidazolium chloride); XRD, X-ray diffraction; XPS, X-ray photoelectron spectroscopy.

was subjected to X-raydiffraction (XRD) test. As shown in **Figure 2C**; **Supplementary Figure 7**, a strong reflection peak was observed in allGO/PIL and rGO/PIL nanocomposite films in the range of 9°-12° and 22.5°-27.5°, respectively, corresponding to their interlayer distances (*d*-spacing, calculated in **Supplementary Table 1**). Along the addition of more PIL, the *d*-spacing was noticed to expand from 0.827 nm for the pristine GO film stepwise to 0.856 nm for GO/PIL-5% (**Figure 2C**), indicating that the introduction of PIL into laminated GO sheets changes the interlayer spacing and induces the structural disorder in GO films. After reduction of GO by HI, the *d*-spacing of GO/PIL-5% narrowed down to only 0.373 nm (**Supplementary Figure 7**) due to the elimination of most oxygenated functionalities on the GO surface; this value is expectedly larger than the pristine rGO film (*d*-spacing ∼ 0.370 nm) due to the introduced PIL chains (**Supplementary Table 1**).

The effect of PIL chains on laminated nanocomposites is further studied *via* Raman spectroscopy (**Figure 2D**). The peak intensity ratio of the D band to the G band (I_D/I_G) increased from 1.07 for GO/PIL-3% to 1.45 for rGO/PIL-3% (**Supplementary Table 2**). These results, together with the decrease of the interlayer spacing after reduction (**Supplementary Table 1**), indicate the removal of oxygenated groups and the partial restoration of sp^2-hybridized carbon networks after HI reduction (Moon et al., 2010; Zhang et al., 2014). The analogous I_D/I_G values of rGO (1.54) and rGO/PIL-3% films suggest that the conjugated π-electron structure of graphitic planes remains nearly intact after the insertion of PIL chains, which is beneficial for the electrical conductivity as discussed later.

X-ray photoelectron spectroscopy (XPS) was employed to extract surface-structural information. As displayed in **Figure 2E**; **Supplementary Figure 8**, the pristine GO film has two typical intense peaks at 287 (C 1s) and 532 eV (O 1s) (Xue et al., 2017), which are similar to GO/PIL-3%. Both GO/PIL-3% and PIL exhibit broad nitrogen signals around 400 eV (N 1s, **Figure 2E**). The N1s spectrum of GO/PIL-3% with two characteristic peaks at 401.3 and 399.5 eV are observed in **Figure 2F**, which are ascribed to the imidazolium N^+ and imidazolium N of the PIL introduced into nanocomposite (Dong et al., 2020). In addition, after HI reduction, the atomic ratios

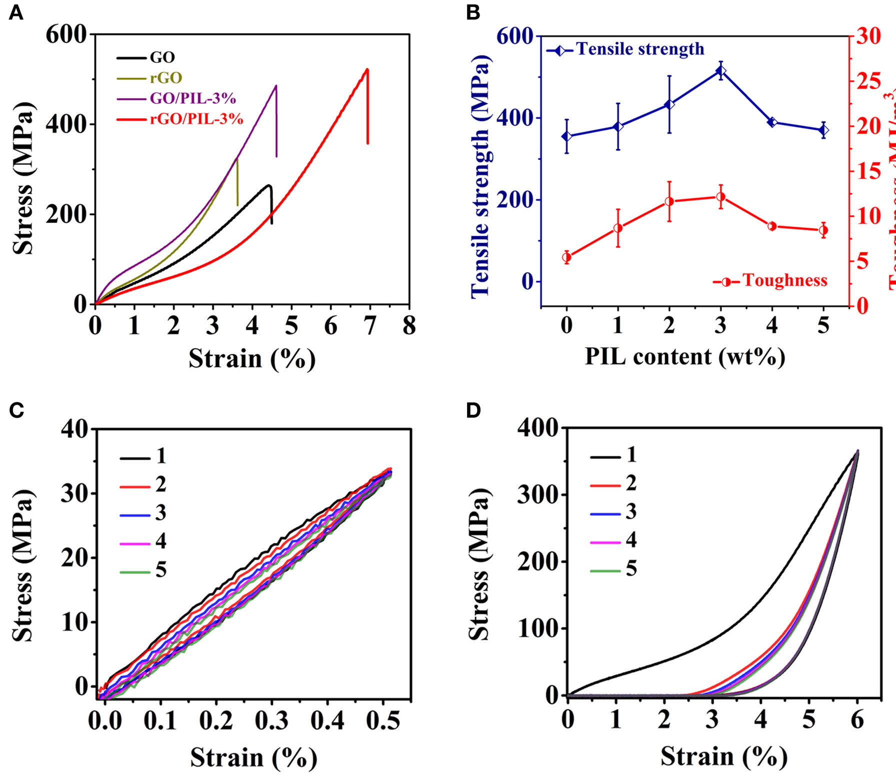

FIGURE 3 | (A) Tensile stress–strain plots of the pristine GO film, rGO film, GO/PIL-3%, and rGO/PIL-3%. **(B)**The tensile strength and toughness of rGO/PIL-***x***% with varied PIL contents, ***x*** = 0 to 5, rGO/PIL-0% is rGO film. Stress–strain curves of rGO/PIL-3% with strain of 0.5% **(C)** and 6.0% **(D)** under five successive loading–unloading cycles. GO, graphene oxide; rGO, reduced graphene oxide; PIL, poly(1-benzyl-3-vinylimidazolium chloride).

of O1s to C1s for both pristine rGO film and the rGO/PIL-3% are lower than those of pristine GO film and the GO/PIL-3% (**Supplementary Figure 8**; **Supplementary Table 2**), respectively, due to the effective elimination of oxygenated groups on the surface of GO nanosheets.

As for the mechanical properties, the typical tensile stress–strain curves of GO, rGO, GO/PIL-3%, and rGO/PIL-3% nanocomposites were measured and shown in **Figure 3A**. The pristine GO film possesses a tensile strength of 253 ± 16 MPa and a toughness of 5.19 ± 0.43 MJ m^{-3}, both of which are higher than the conventional GO films prepared from GO nanosheets that are made by the classic Hummers method (Chen et al., 2019). This is because that in our samples, the room-temperature oxidation of nature graphite is mild to limit structure defects so as to generate larger graphitic domains than conventional GOs. This difference results in stronger intersheet interactions. After HI reduction, the tensile strength and toughness of polymer-free rGO film increased to 355 ± 41 MPa and 5.44 ± 0.70 MJ m^{-3}, respectively. This improvement is supposed to stem from amplified π-π interaction between adjacent rGO sheets caused by narrower *d*-spacing after reduction by HI, as confirmed by XRD and Raman analyses mentioned above (**Supplementary Figure 7**; **Figure 2D**).

At a microscopic level, when PIL was introduced into GO nanosheets, as designed, the imidazolium cation and the phenyl group could construct strong cation–π and π-πinteractions, respectively, with GO. Besides, the imidazolium cation and its associated counter anion (Cl^-) could interact in addition with oxygenated groups on GO nanosheets *via* electrostatic interactions and hydrogen bonding, respectively (Yin et al., 2017). Owing to these multiple supramolecular interactions introduced by PIL into the nanocomposite, GO/PIL-3% nanocomposite shows a simultaneously enhanced tensile strength of 492 ± 52 MPa and toughness of 8.81 ±1.12 MJ m^{-3}, respectively (**Supplementary Figure 9**).

In control experiment, we synthesized a phenyl-freeimidazolium-based analog poly(ionic liquid), poly(3-cyanomethyl-1-vinylimidazolium bromide) (termed, PILC) (**Supplementary Figure 10**). Here, the phenyl group was replaced by a nitrile group so as to reduce the aromatic nature of PILC. Such polymer interaction with the adjacent GO nanosheets *via* similar supramolecular interactions, in which the π-π interaction between GO nanosheets and PILC, however disappears. As shown in **Supplementary Figure 11**; **Supplementary Table 3**, the maximum tensile strength and toughness reach only 357 ± 33 MPa and 7.08 ± 0.95 MJ m^{-3}, respectively, which are 20–30% less than the GO/PIL-3% film, though higher than the pristine GO film. Therefore, not only the cation but also the phenyl groups are crucial to the mechanical properties of the composites.

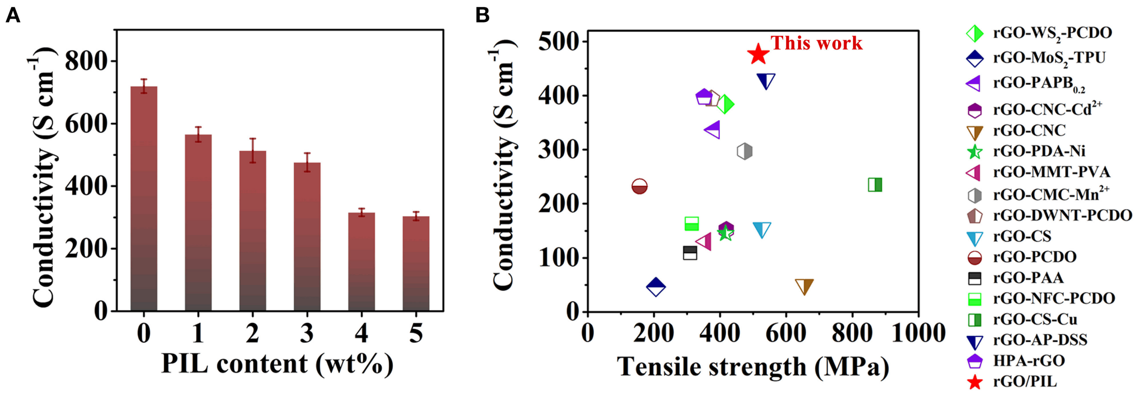

FIGURE 4 | (A) The electrical conductivity of rGO/PIL-***x***%, x = 0 to 5, rGO/PIL-0% is rGO film. **(B)** Comparison of mechanical and electrical properties of rGO/PIL-3% and other rGO-based nanocomposites known in literature. GO, graphene oxide; rGO, reduced graphene oxide; PIL, poly(1-benzyl-3-vinylimidazolium chloride).

After HI reduction of the carboxylate and hydroxyl groups on GO surface, imidazolium-carboxylate-based electrostatic attraction and hydrogen bonding could forfeit in large part, while the π-π and cation–π interactions between PIL and rGO are believed to remain, and in fact to increase in the rGO/PIL composite due to partial recovery of π-conjugated networks as well as the narrower inter-layer distance. We tested the tensile strength and toughness of rGO/PIL nanocomposite with different PIL contents (**Figure 3B**; **Supplementary Figure 12**). Among all samples, rGO/PIL-3% reaches the highest tensile strength of 516 ± 22 MPa and toughness of 12.16 ± 1.31 MJ m^{-3}, respectively, which are 1.5 and 2.2 times of that for the pristine rGO film, and also higher than the GO/PIL-3%. To note, the overloading of PIL above 3 wt% weakens the mechanical properties of nanocomposite films since the overloading of PIL in the nanocomposites would form some bulk polymer domains of less strength and toughness than GO, and meanwhile such polymer domains will deteriorate the regular packing of GO nanosheets. The detailed mechanical property data are listed in **Supplementary Table 4**.

Clearly, the high mechanical properties of rGO/PIL-3% are mainly attributed to a synergistic effect from the π-π and cation–π interactions between PIL and rGO and the amplified π-π interactions between rGO sheets themselves, which are further confirmed by cyclic stress–strain measurements, as shown in **Figures 3C,D**. Initially, the cyclic loading–unloading within a small strain of 0.5% obtains a reversible deformation of rGO/PIL-3%, indicating an elastic deformation (**Figure 3C**). At a higher strain of 6.0% (**Figure 3D**), rGO/PIL-3% was stretched with a permanent deformation of 2.9% after five successive loading–unloading cycles, which exhibits a plastic characteristic. During this stretching process, π-π and cation–π interactions between PIL and rGO are gradually broken, leading to continuous slippage between adjacent rGO nanosheets along the stretching direction. Therefore, the phenyl group and the imidazolium cation in PIL enable an optimal crosslinking strategy for dissipating a large amount of energy during tensile deformation, synergistically strengthening and toughening rGO films.

Much different from the GO/PIL composites, all rGO/PIL composites are electron conductive with the measured conductivity ranging from 565 ± 24S cm^{-1} for rGO/PIL-1% to 304 ± 14 S cm^{-1} for rGO/PIL-5% (**Supplementary Table 4**). Carrying the greatest mechanical properties, the rGO/PIL-3% nanocomposite has also an excellent electrical conductivity of 476 ± 30 S cm^{-1}, with respect to pristine rGO of 720 ± 22 S cm^{-1}, as shown in **Figure 4A**. Considering both excellent electrical and mechanical properties, rGO/PIL-3% exhibits integrated high performance compared with most previously reported rGO-based nanocomposites, as shown in **Figure 4B**; **Supplementary Table 5**. This result also indicates that the PIL with encoded organic functionalities do not disrupt the π-conjugated domains of rGO, preserving in large part the electrical properties. Meanwhile, the mechanical and electrical properties could remain stable in certain extent under relatively high working temperature (at least 100°C), as shown in **Supplementary Figure 13**. Hence excellent strength and toughness combined with a high electrical conductivity enable potential applications in e.g., flexible and wearable electronic devices.

CONCLUSIONS

In this work, we developed a new fabrication strategy for rGO composite films containing a PIL with a phenyl and an imidazolium cation in the repeating unit, possessing ultrahigh strength and toughness as well as high electrical conductivity. The unique chemical structure of PIL could effectively reinforce the rGO composite films *via* synergistic cation–π and π-π interactions. This high-performance rGO/PIL nanocomposite is promising for applications in many fields, such as aerospace, artificial muscles, tissue engineering, and especially flexible electrodes due to its high electrical conductivity.

DATA AVAILABILITY STATEMENT

The original contributions presented in the study are included in the article/**Supplementary Material**, further inquiries can be directed to the corresponding author/s.

AUTHOR CONTRIBUTIONS

JC, MZ, and JY contributed to the conception of the study and performed the data analyses and wrote the manuscript. JC performed the laboratory experiments. JC, MZ, XZ, WC, QZ, and JY contributed significantly to the analysis and manuscript preparation. All authors contributed to the article and approved the submitted version.

FUNDING

JY is grateful for financial support from European Research Council (ERC) Starting Grant NAPOLI-639720, Swedish Research Council Grant 2018-05351, Dozentenpreis 15126 from Verband der Chemischen Industrie e.V. (VCI) in Germany, the Wallenberg Academy Fellow program (Grant KAW 2017.0166) in Sweden, and the Stockholm University Strategic Fund SU FV-2.1.1-005.

SUPPLEMENTARY MATERIAL

The Supplementary Material for this article can be found online at: https://www.frontiersin.org/articles/10.3389/fmats.2021.635987/full#supplementary-material

REFERENCES

Barthelat, F., Yin, Z., and Buehler, M. J. (2016). Structure and mechanics of interfaces in biological materials. *Nat. Rev. Mater.* 1, 16007. doi: 10.1038/natrevmats.2016.7

Chen, H., Du, W., Liu, J., Qu, L., and Li, C. (2019). Efficient room-temperature production of high-quality graphene by introducing removable oxygen functional groups to the precursor. *Chem. Sci.* 10, 1244–1253. doi: 10.1039/C8SC03695K

Cheng, Q., Duan, J., Zhang, Q., and Jiang, L. (2015). Learning from nature: constructing integrated graphene-based artificial nacre. *ACS Nano* 9, 2231–2234. doi: 10.1021/acsnano.5b01126

Cheng, Q., Wu, M., Li, M., Jiang, L., and Tang, Z. (2013). Ultratough artificial nacre based on conjugated cross-linked graphene oxide. *Angew. Chem. Int. Ed.* 52, 3750–3755. doi: 10.1002/anie.201210166

Cui, W., Li, M., Liu, J., Wang, B., Zhang, C., Jiang, L., et al. (2014). A strong integrated strength and toughness artificial nacre based on dopamine cross-linked graphene oxide. *ACS Nano* 8, 9511–9517. doi: 10.1021/nn503755c

Dong, Z., Zhang, C., Huawen, P., Gong, J., Wang, H., Zhao, Q., et al. (2020). A cationitrile sequence encodes mild poly (ionic liquid) crosslinking for advanced composite membranes. *Mater. Horiz.* 7, 2683. doi: 10.1039/D0MH00795A

Grygiel, K., Lee, J.-S., Sakaushi, K., Antonietti, M., and Yuan, J. (2015). Thiazolium poly (ionic liquid)s: synthesis and application as binder for lithium-ion batteries. *Acc. Mater. Res.* 4, 1312–1316. doi: 10.1021/acsmacrolett.5b00655

Huang, G., Han, D., Jin, Y., Song, P., Yan, Q., and Gao, C. (2018). Fabrication of nitrogen-doped graphene decorated with organophosphor and lanthanum toward high-performance ABS nanocomposites. *ACS Appl. Nano Mater.* 1, 3204–3213. doi: 10.1021/acsanm.8b00411

Huang, G., Huo, S., Xu, X., Chen, W., Jin, Y., Li, R., et al. (2019). Realizing simultaneous improvements in mechanical strength, flame retardancy and smoke suppression of ABS nanocomposites from multifunctional graphene. *Compos. B. Eng.* 177:107377. doi: 10.1016/j.compositesb.2019.107377

Kulkarni, D. D., Choi, I., Singamaneni, S. S., and Tsukruk, V. V. (2010). Graphene oxide-polyelectrolyte nanomembranes. *ACS Nano* 4, 4667–4676. doi: 10.1021/nn101204d

Li, Y., Xue, Z., Luan, Y., Wang, L., Zhao, D., Xu, F., et al. (2019). Improved mechanical performance of graphene oxide based artificial nacre composites by regulating the micro-laminated structure and interface bonding. *Compos. Sci. Technol.* 179, 63–68. doi: 10.1016/j.compscitech.2019.04.032

Liu, L., Gao, Y., Liu, Q., Kuang, J., Zhou, D., Ju, S., et al. (2013). High mechanical performance of layered graphene oxide/poly (vinyl alcohol) nanocomposite films. *Small* 9, 2466–2472. doi: 10.1002/smll.201300819

Men, Y., Drechsler, M., and Yuan, J. (2013). Double-stimuli-responsive spherical polymer brushes with a poly (ionic liquid) core and a thermoresponsive shell. *Macromol. Rapid Commun.* 34, 1721–1727. doi: 10.1002/marc.201300628

Moon, I. K., Lee, J., Ruoff, R. S., and Lee, H. (2010). Reduced graphene oxide by chemical graphitization. *Nat. Commun.* 1:73. doi: 10.1038/ncomms1067

Park, S., Lee, K.-S., Bozoklu, G., Cai, W., Nguyen, S. T., and Ruoff, R. S. (2008). Graphene oxide papers modified by divalent ions-enhancing mechanical properties via chemical cross-linking. *ACS Nano* 2, 572–578. doi: 10.1021/nn700349a

Schniepp, H. C., Li, J.-L., McAllister, M. J., Sai, H., Herrera-Alonso, M., Adamson, D. H., et al. (2006). Functionalized single graphene sheets derived from splitting graphite oxide. *J. Phys. Chem. B* 110, 8535–8539. doi: 10.1021/jp060936f

Shao, Y., Wang, Y. L., Li, X., Kheirabad, A. K., Zhao, Q., Yuan, J., et al. (2020). Crosslinking of a single poly (ionic liquid) by water into porous supramolecular membranes. *Angew. Chem. Int. Ed.* 59, 17187–17191. doi: 10.1002/anie.202002679

Song, P., Xu, Z., Wu, Y., Cheng, Q., Guo, Q., and Wang, H. (2017). Super-tough artificial nacre based on graphene oxide via synergistic interface interactions of π-π stacking and hydrogen bonding. *Carbon* 111, 807–812. doi: 10.1016/j.carbon.2016.10.067

Tan, Z., Zhang, M., Li, C., Yu, S., and Shi, G. (2015). A general route to robust nacre-like graphene oxide films. *ACS Appl. Mater. Interfaces* 7, 15010–15016. doi: 10.1021/acsami.5b04093

Wan, S., Hu, H., Peng, J., Li, Y., Fan, Y., Jiang, L., et al. (2016). Nacre-inspired integrated strong and tough reduced graphene oxide-poly (acrylic acid) nanocomposites. *Nanoscale* 8, 5649–5656. doi: 10.1039/C6NR00562D

Wang, J., Qiao, J., Wang, J., Zhu, Y., and Jiang, L. (2015). Bioinspired hierarchical alumina-graphene oxide-poly (vinyl alcohol) artificial nacre with optimized strength and toughness. *ACS Appl. Mater. Interfaces* 7, 9281–9286. doi: 10.1021/acsami.5b02194

Wang, X., and Shi, G. (2015). Flexible graphene devices related to energy conversion and storage. *Energy Environ. Sci.* 8, 790–823. doi: 10.1039/C4EE03685A

Wang, Y., Li, T., Ma, P., Zhang, S., Zhang, H., Du, M., et al. (2018). Artificial nacre from supramolecular assembly of graphene oxide. *ACS Nano* 12, 6228–6235. doi: 10.1021/acsnano.8b03025

Wang, Y., Shao, Y., Wang, H., and Yuan, J. (2020). Advanced heteroatom-doped porous carbon membranes assisted by poly (ionic liquid) design and engineering. *Acc. Mater. Res.* 1, 16–29. doi: 10.1021/accountsmr.0c00010

Woo, J. Y., Oh, J. H., Jo, S., and Han, C.-S. (2019). Nacre-mimetic graphene oxide/cross-linking agent composite films with superior mechanical properties. *ACS Nano* 13, 4522–4529. doi: 10.1021/acsnano.9b00158

Xu, Z., Song, P., Zhang, J., Guo, Q., and Mai, Y.-W. (2018). Epoxy nanocomposites simultaneously strengthened and toughened by hybridization with graphene oxide and block ionomer. *Compos. Sci. Technol.* 168, 363–370. doi: 10.1016/j.compscitech.2018.10.020

Xue, Z., Huang, P., Li, T., Qin, P., Xiao, D., Liu, M., et al. (2017). A novel "tunnel-like" cyclopalladated arylimine catalyst immobilized on graphene oxide nano-sheet. *Nanoscale* 9, 781–791. doi: 10.1039/C6NR07521E

Yin, B., Zhang, X., Zhang, X., Wang, J., Wen, Y., Jia, H., et al. (2017). Ionic liquid functionalized graphene oxide for enhancement of styrene-butadiene rubber nanocomposites. *Polym. Adv. Technol.* 28, 293–302. doi: 10.1002/pat.3886

Zhang, M., Huang, L., Chen, J., Li, C., and Shi, G. (2014). Ultratough, ultrastrong, and highly conductive graphene films with arbitrary sizes. *Adv. Mater.* 26, 7588–7592. doi: 10.1002/adma.201403322

Zhang, M., Wang, Y., Huang, L., Xu, Z., Li, C., and Shi, G. (2015). Multifunctional pristine chemically modified graphene films as strong as stainless steel. *Adv. Mater.* 27, 6708–6713. doi: 10.1002/adma.201503045

Zhang, S. Y., Miao, H., Zhang, H. M., Zhou, J. H., Zhuang, Q., Zeng, Y. J., et al. (2020). Accelerating crystallization of open organic materials by poly (ionic liquid)s. *Angew. Chem. Int. Ed.* 59, 22109–22116. doi: 10.1002/anie.202008415

Zhang, Y., Gong, S., Zhang, Q., Ming, P., Wan, S., Peng, J., et al. (2016). Graphene-based artificial nacre nanocomposites. *Chem. Soc. Rev.* 45, 2378–2395. doi: 10.1039/C5CS00258C

Zhao, G., and Zhu, H. (2020). Cation-π interactions in graphene-containing systems for water treatment and beyond. *Adv. Mater.* 32:1905756. doi: 10.1002/adma.201905756

Zhao, H., Yue, Y., Zhang, Y., Li, L., and Guo, L. (2016). Ternary artificial nacre reinforced by ultrathin amorphous alumina with exceptional mechanical properties. *Adv. Mater.* 28, 2037–2042. doi: 10.1002/adma.201505511

Conflict of Interest: The authors declare that the research was conducted in the absence of any commercial or financial relationships that could be construed as a potential conflict of interest.